1 **Profiling the size-dependent heterogeneity of membrane proteins in a**

2 **mixed population of small extracellular vesicle for potential cancer**

3 **diagnosis**

4

5

6 Chunhui Zhai[1], Feng Xie[1], Qiang Zeng[1], Weiqiang Zheng[2], Jingan Wang[1], Haiyan

7 Hu[3], Yuting Yang[2, *], Xianting Ding[1, 4, *], Hui Yu[1, 4, *]

8

9 [1] Institute for Personalized Medicine, School of Biomedical Engineering, Shanghai

10 Jiao Tong University, Shanghai, 200030, People's Republic of China.

11 [2] Department of Instrument Science and Engineering, School of Electronic

12 Information and Electrical Engineering, Shanghai Jiao Tong University, Shanghai,

13 200030, People's Republic of China.

14 [3] Oncology Department of Shanghai Jiao Tong University Affiliated Sixth People's

15 Hospital

16 Shanghai, 200233, People's Republic of China.

17 [4] Institute of Medical Robotics, Shanghai Jiao Tong University, Shanghai, 200030,

18 People's Republic of China.

19
20 *Corresponding author. E-mail: hui.yu@sjtu.edu.cn (Prof. Hui Yu);
21 yuting.bme@sjtu.edu.cn (Prof. Yuting Yang); dingxianting@sjtu.edu.cn (Prof.
22 Xianting Ding)

23
24 **Abstract**

25
26 The heterogeneity in small extracellular vesicles (small EVs) introduces an extra level
27 of complexity in small EV-based liquid biopsy for cancer diagnosis. Heterogeneous
28 membrane protein expression is correlated with sizes of small EVs, but accessing this
29 correlative information is limited by the precise isolation of size-dependent
30 subpopulations. Herein, we present a single EV enumeration (SEVEN) approach to
31 profile protein heterogeneity in size-dependent subpopulations, and demonstrate its
32 potential in improving the accuracy of cancer diagnosis. The interferometric plasmonic
33 microscopy (iPM) capable of imaging single biological nanoparticles with the diameter
34 down to 30 nm is employed to detect small EVs at the single-particle level. Small EVs
35 population with mixed sizes are directly imaged, individually sized and digitally

counted during their binding onto different aptamer-coated iPM sensor surfaces. The protein expression levels and binding kinetics of three size-dependent subpopulations are analyzed, forming a multidimensional data matrix for cancer diagnosis. Using small EVs derived from different cancer cell lines, highly heterogeneous protein profiles are recorded in the three subpopulations. We further demonstrate that the cancer classification accuracy could be greatly improved by including the subpopulation level heterogeneous protein profiles as compared with conventional ensemble measurement.

MAIN TEXT

Introduction

Extracellular vesicles (EV) are a group of membrane-enclosed phospholipid vesicles secreted by mammalian cells, including normal cells as well as cancer cells[1]. Small EV (sEV), including exosomes and a portion of microvesicles, is a unique subset with a diameter of less than 200 nm[2]. EVs, including sEV, are packaged with functional molecules (i.e. proteins, amino acids and nucleic acids) of their parental cells, and play an important role in cell-cell communication[3], immune response[4] and cancer metastasis[5][6]. sEV are highly heterogeneous in the membrane proteins, sizes and contents depending on the cell sources, cancer-gene mutation and other environmental factors[7][8][9], making them a potential tool in cancer diagnosis[10][11]. For example, by profiling the expression level of membrane proteins from sEV, early diagnosis of breast cancer[12][13] and classification of cancer types[14] have been demonstrated.

With sophisticated isolation techniques, size-dependent subsets of sEV including exomere (<50 nm), Exo-S (60 - 80 nm) and Exo-L (90 - 120 nm) were identified with unique molecular biomarker profiles[15]. This suggests that conventional analytical approaches by measuring average information from the full population of sEV would inevitably suffer from the large background noise from irrelevant subpopulations[16]. Profiling protein heterogeneity of the size-dependent sEV subpopulations would thus largely advance our knowledge in the mechanism of their biological functions, as well as the development of accurate diagnostic tools[8]. However, the major challenge to access the heterogeneity information is the difficulties in precisely isolation of sEV subpopulations with specific sizes. Although there are several emerging techniques for

68   isolation of sEV subpopulations [15] [17] [18] [19] [20] [21] [22], they typically suffer from poor

69   efficiency, time consuming process, and sophisticated fabrication[23].

70   Herein, we present an alternative approach termed single EV enumeration (SEVEN)

71   to profiling the protein heterogeneity in size-dependent subsets of small EVs for cancer

72   diagnosis. Instead of profiling proteins on isolated size-dependent subsets in the

73   conventional approaches, SEVEN accurately sizes single small EVs captured by

74   different aptamers to access the heterogeneity information. Using small EVs derived

75   from five different cancer cell lines, we measured the heterogeneous expression of five

76   different membrane proteins on three small EVs' subsets, and developed a machine

77   learning algorithm for cancer classification.

78

79   **Results and Discussions**

80

81   **The overview of SEVEN.**

82   The principle of SEVEN is based on our previous work to image, size and digitally

83   count single sEV by the interferometric plasmonic microscopy (iPM)[24] [25] (**Figure 1**).

84   For each protein biomarker detection, SEVEN dynamically measures the size of each

85   sEV particle specifically binding onto an aptamer-coated sensor surface (**Table S1**),

86   and divides them into size-dependent subpopulations. Corresponding size-dependent

87   binding curves are then constructed by digital counting of sEV, from which parameters

88   including the maximum binding number and the exponential coefficient are quantified.

89   For sEV from different cell sources measured on different aptamer-coated sensor

90   surfaces, these parameters form a multidimensional matrix containing size-dependent

91   heterogeneous information of protein biomarkers.

92
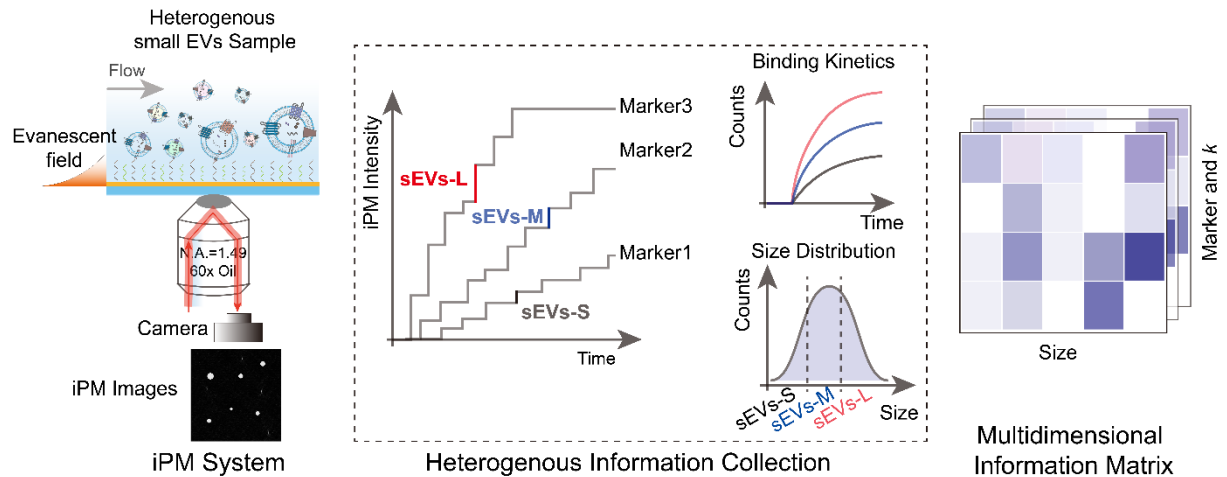
Figure 1. The schematics. Binding of sEV onto specific aptamer-coated sensors is imaged with the iPM system; image intensity and counts are analyzed to construct binding curves of each subpopulation (sEV-L, sEV-M and sEV-S); a matrix is formed with the sizes, counts and kinetics.

Verification of sEV sample.

Five different cell lines, including A549 (lung cancer), HepG2 (liver cancer), MCF-7 (breast cancer), LNCaP (prostatic cancer) and L-02 (normal liver cells), were cultured to derive sEV. sEV were isolated from the culture medium using ultracentrifugation methods as described previously[26]. The sizes of isolated EVs were below 200 nm as measured by nanoparticle tracking analysis (NTA) (**Figure 2a** and **Figure S1**), and the concentration varied from 10^{10} /mL to 10^{12} /mL. The morphology of sEV was characterized by transmission electron microscopy (TEM), showing typical entire and saucer-like shapes (**Figure 2b**). According to the guidelines in minimal information for studies of extracellular vesicles 2018 (MISEV 2018)[27], we found that three universal EV-positive plasma membrane proteins, Alix, CD63 and Tsg101 were positively expressed, and one EV-negative protein, Calnexin, was negatively expressed with western blot (**Figure 2c**).
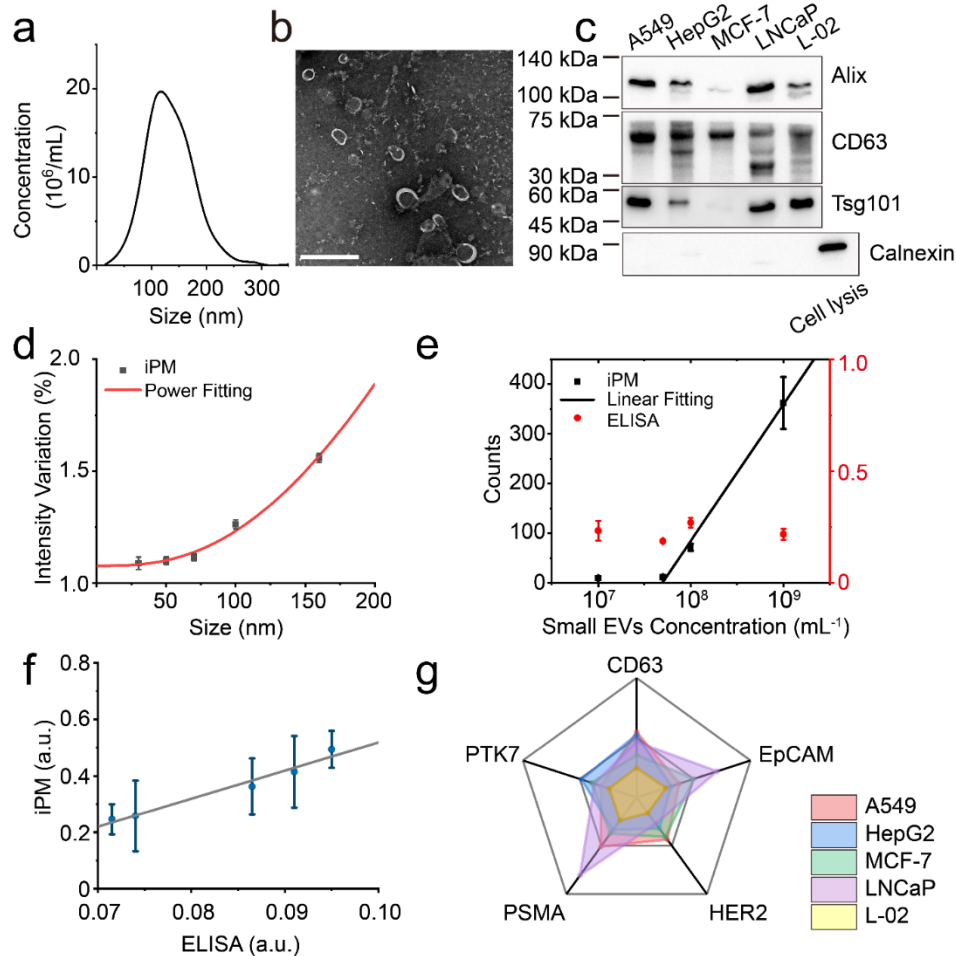
Figure 2. Single sEV imaging and detection. (a) Concentration and size distribution of A549-derived sEV measured by NTA. (b) Typical TEM images of sEV. (c) Western blot results of Alix, CD63, Tsg101 and Calnexin in sEV derived from A549, HepG2, MCF-7, LNCaP, L-02 cell lines. (d) Theoretical (red) and experimental (black) iPM intensities of silica nanoparticles of 30 nm, 50 nm, 70 nm, 100 nm, and 160 nm. (e) Sensitivity of iPM (black) and ELISA (red) for the detection of sEV from MCF-7 cells with CD63 aptamer -coated sensor chips. (f) CD-63 level on sEV of five cells lines determined by iPM and ELISA. (g) Radar plot showing iPM analyses of 5 EV protein markers from the five different cell lines (n = 3).

Plasmonic imaging and detection of sEV.

In SEVEN, the iPM system offers a unique approach to image and characterize single sEV. After binding onto the chips, sEV showed an intact morphology as characterized by scanning electron microscope (SEM) (**Figure S2**). We established the calibration curve between iPM intensity and particle sizes using silica nanoparticles (**Figure 2d** and **Figure S3**), and measured the sizes of sEV by intercalation. Using sEV samples from MCF-7 as an example, the number of EVs binding onto optimized HER2-aptamer

131   modified sensor surfaces (**Figure S4)** within 15 minutes correlated well with the

132   concentrations of total sEV in the range from 5×10^7 /mL to 10^9 /mL (**Figure 2e**). The

133   specificity in measuring HER2-positive sEV was verified by comparing the binding on

134   bull serum albumin (BSA)-coated surface and a dissociation experiment (**Figure S5**).

135   Note that the conventional enzyme-linked immunosorbent assay (ELISA) failed to

136   measure the HER2-positive sEV due to insufficient sensitivity.

137   Besides measuring the size and concentration, SEVEN could also report the average

138   level of specific proteins in sEV samples. For sEV samples of the five cell lines at the

139   concentration of 2×10^{10} /mL, we compared the CD63 expression levels measured by

140   ELISA with the percentage of CD63-positive EVs in total EVs determined by iPM,

141   which showed a good linear correlation ($R^2 > 0.96$, **Figure 2f**). Similarly, the expression

142   levels of protein biomarkers in the sEV from five cell lines were measured as the

143   percentage of target-specific EVs, which were largely different from each other (**Figure**

144   **2g**). We note that the protein levels reported by SEVEN are not the expression level on

145   single sEV, by related to the total proteins from the all sEV.

146

147   **Limitations in cancer diagnosis by total sEV analysis.**

148   We then explored the capability of SEVEN in profiling proteins in total sEV population

149   for cancer diagnosis, which is the common practice. 72 small EV samples were

150   collected from the cancer cell lines of A549, HepG2, MCF-7 and LNCaP, and 18

151   samples were collected from L-02 healthy liver cell lines as the control. The expression

152   of the five biomarkers was first confirmed by Western blot (**Figure 2c** and **Figure S6**).

153   Expression levels of CD63, EpCAM, HER2, PSMA and PTK7 in the small EV samples

154   from the five cell lines were measured as the percentage of target-positive EVs in total

155   EVs as described above (**Figure 3a**). The heterogeneity among different batches of

156   small EV samples was obvious, which is inevitable due to the intrinsic variations in cell

157   conditions and other environmental factors. The exponential coefficients related to the

158   association rates were quantified, which were also heterogeneous among difference cell

159   lines (**Figure 3b**).

160   sEV from the four cancer cell lines showed a significantly higher protein levels than

161   the healthy control from L-02 ($p < 0.01$, **Figure 3c**), indicating the potential to perform

162   cancer diagnosis with these biomarkers. But when performing the cancer classification

163   with the expression level and exponential coefficient of only one of the biomarkers,

164   none was able to classify all five cancers with $p < 0.05$ (**Figure 3d**) in a pairwise

165   comparison. Even the well-recognized specific markers, such as HER2 and PSMA,

166   were not able to distinguish breast cancer and prostate cancer. When the expression

167   levels and exponential coefficients of all five biomarkers were analyzed with the Linear

168   Discriminant Analysis (LDA) algorithm used in previous study[13], the overall average

169   classification accuracy was only 34% (**Figure 3e** and **Figure S10 c**). The areas under

170   the curve (AUC) were 0.74, 0.48, 0.64, 0.56 and 0.85 respectively, using receiver

171   operating characteristic (ROC) analysis (**Figure 3f**).

172
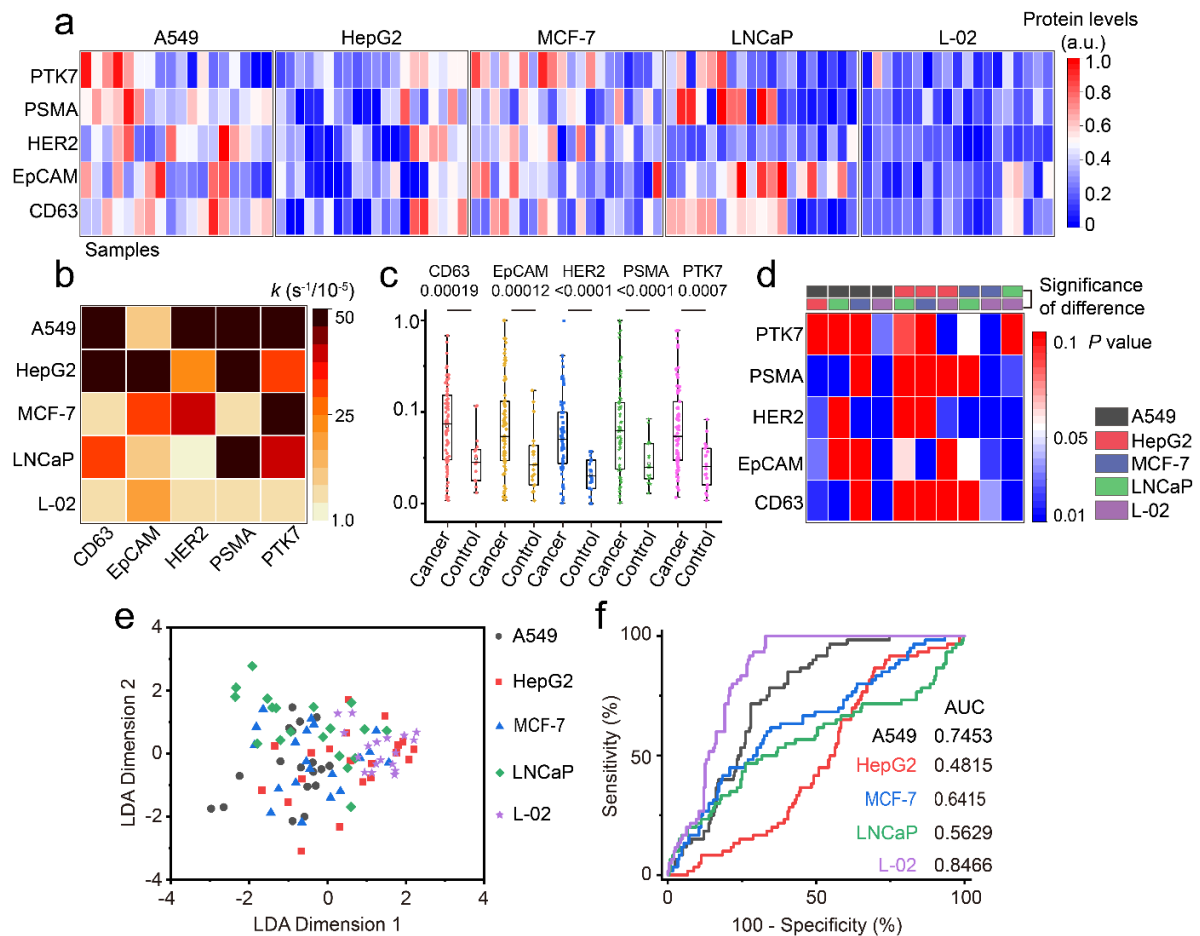
174 **Figure 3. Profiling total sEV surface protein markers.** (a) Heat map of sEV surface

175 protein in 5 cell lines (18 samples for each cancer cell line). (b) The association rates

176 of total sEV from five cell lines. (c) Elevated protein levels of all 5 protein markers in
177 sEV derived from cancer cell lines (n = 78; means ± s.e.m.) than normal cell line
178 (n = 18; means ± s.e.m.). (d) The statistical differences in distinguishing cancer types
179 (n = 18 samples for each cell type) by a single biomarker by independent samples t-test.
180 (e) Cancer classification using five protein biomarkers of total sEV by LDA. (f) The
181 ROC curves for cancer classification in (e).

182

183 These results suggest that using protein biomarkers in the mix population of sEV could

184 lead to poor accuracy in the cancer diagnosis. One of the reasons could be due to the

185 heterogeneity at the single EV level. For example, when examining the CD63 level in

186 sEV from LNCaP cells using immunoelectron microscopy, different number of

187 immuno-gold nanoparticles were observed on sEV (**Figure S7**). We then investigated

188 the possibility to improve cancer diagnosis accuracy by exploring the protein

189 heterogeneity at the subpopulation level.

190 **Profiling protein heterogeneity in size-dependent subpopulations**.

191 The sEVs were empirically divided into three size-dependent subpopulations, including

192 the sEV-S (30-70 nm), sEV-M (70-120 nm) and sEV-L (120-160 nm). With the single

193 EVs imaging and sizing capability of iPM, the binding curves of three subpopulations

194 were digitally plotted (**Figure 4a** and **Figure S8**). The exponential coefficients were

195 obviously heterogeneous (**Figure 4b**). For example, the exponential coefficients were

196 0.0070, 0.0091, and 0.0089 s^{-1} for sEV-S, sEV-M and sEV-L binding with PSMA-

197 aptamer, and 0.0013, 0.0015, and 0.0028 s^{-1} with CD63-aptamer respectively, and

198 LNCaP and L-02 derived sEV showed much faster binding rates than A549-derived

199 sEV.

200
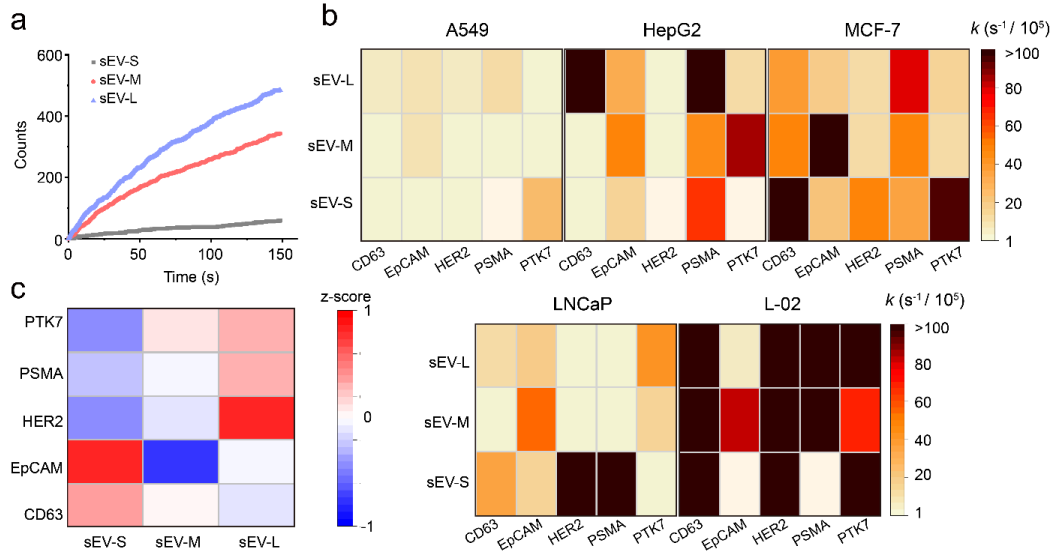
Figure 4. Binding kinetics and distinct marker of size-dependent sEV's subpopulations. (a), An example of binding curves of LNCaP-derived sEV subpopulations on PSMA-modified chips. (b), The heat map of apparent association rate k of five kind of cell lines in five kind of aptamers-modified sensor chips. (c), Heatmap illustration of the relative abundance of sEV (A549) markers in sEV-S, sEV-M and sEV-L. Scale shown is protein levels subtracted by mean and divided by row standard deviation (that is, Δ (protein levels − mean)/s.d.).

We further calculate the z score of protein levels from the three subpopulations to highlight the difference[15]. In sEV from all cell lines other than A549, all protein markers were found to enrich in sEV-L (Figure S9). While for A549, EpCAM and CD63 were mainly expressed in the sEV-S subpopulations, but HER2, PSMA and PTK7 in sEV-L (Figure 4c). This confirms that membrane protein expression levels in sEV are not directly proportional to membrane areas, but instead, they were packaged purposely. The reason why specifically only EpCAM and CD63 from A549 cells were highly expressed in sEV-S is still unknown. Note that the sEV-s population weighed only a small portion of the total sEV (Figure 2a). Thus, when analyzing EpCAM and CD63 from the total sEV, the majority as sEV-M and sEV-L would give a large background noise, which explains the poor accuracy in Figure 3d.

**Improving cancer classification accuracy with subset information.**

The multidimensional information matrixes of sEV, including the protein levels and exponential coefficients of total sEV and those of three subpopulations were input into

225   a LDA model to discriminate the five cell lines (**Figure 5a**). Using the same raw data

226   and similar LDA algorithms in **Figure 3e**, the overall classification accuracy

227   significantly improved to 70% (**Figure 5b, 5c**), with the AUC of 0.97, 0.85, 0.85, 0.97

228   and 0.82 for the five cell lines, respectively (**Figure 5d**). Precision Recall Curves (PRC)

229   also showed a better performance of classification with subset information comparing

230   to that without subset information to differentiate cancer cell lines (**Figure S10a, b**).

231   Classification patterns of the HepG2 liver cancer cell line and the L-02 healthy liver

232   cell line largely overlapped, but discrimination between cancer cell lines from different

233   origins was reliable. When we combine the data of HepG2 and L-02 into a same group,

234   the average accuracy was improved to over 81% (**Figure S10d**).

235

236
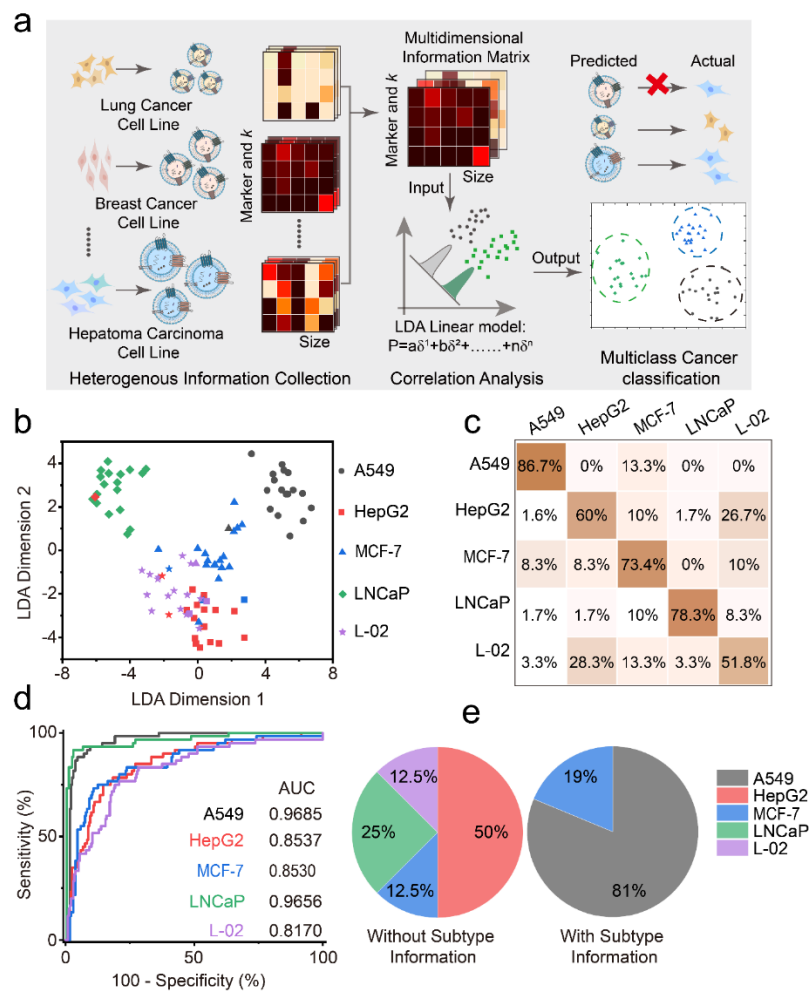
237 **Figure 5. Multiclass cancer classification with subset information.** (a) The

238 workflow of SEVEN-based cancer classification with subset information. (b) The

239 classification results by including subset information into Fig.3e. (c) Probability matrix

240 summarizing the cancer classification results in (b). (d) ROC curves of (c). (e) Results

241 in determining the origin of A549 derived sEV spiked in human serum samples.

242

243 We further performed simple validation experiments by spiking sEV derived from

244 A549 cell lines into EV-depleted serum samples, and determined their origin with

245 SEVEN. The ratio of success reached 81% (**Figure 5e**) with the information at the size-

246 dependent subpopulations, while without this information none was correctly classified.

247 This indicates the potential of SEVEN in analyzing sEV in complicated samples for

248 future clinical applications.

249 **Re-defining the size-dependent subsets of sEV.**

250 Simply dividing the sEV into as small, medium and large subsets is intuitive but brutal,

251 both in previous work by isolating the subsets and in this work by empirically setting

252 thresholds. There has been little evidence showing why the membrane proteins and

253 contents should be packed in such a simple size-dependent manner. A deeper study is

254 hindered by the capability to isolate the sEV subsets within narrower size ranges.

255 However, in SEVEN, the iPM system offers a sizing accuracy of 10 nm, which provides

256 the opportunity to potentially address this problem. We thus re-calculated the SEVEN

257 data between 30 to 160 nm as thirteen subgroups at the interval of 10 nm. Instead of

258 empirically combining some of the subgroups, we developed an artificial intelligent

259 algorithm to automatically search for the optimal size partition to achieve the best

260 classification accuracy (Figure S11). The results show that when the sEV were grouped

261 by sizes within 30-40 nm, 40-100 nm, 100-110 nm, 110-130 nm, 130-140 nm and 140-

262 160 nm, the classification accuracy with raw data in Figure 5 dramatically increased to

263 87% (**Figure 6**). Besides, the healthy liver cell line L-02 was fully separated from

264 cancerous cell lines.

265

266
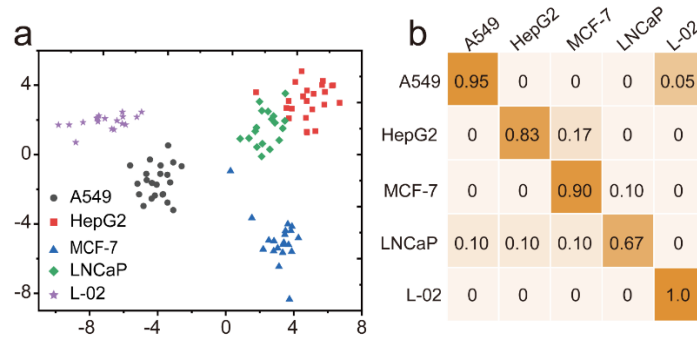
Figure 6 Multiclass cancer classification by re-grouping the subsets. (a) The classification results of five cell lines with raw data in Figure 5. (b) Probability matrix summarizing the cancer classification results in (a).

Discussion

We have presented the single EV enumerating (SEVEN) approach to explore the in-depth information of size-dependent heterogeneity of sEV. Benefits from the single particle imaging and detection capability, SEVEN circumvents the challenges in precise isolation of subpopulations. Studies on five cell lines and five protein biomarkers have provided new evidence in the correlation between the protein levels and the size distribution of sEV. Experiments with sEV from cancer cell lines and those spiked in serum samples show that SEVEN could effectively improve the diagnostic accuracy over ensemble measurements. This work thus has highlighted the importance to explore the underlying relationship between different dimensions of heterogeneity of sEV for developing better diagnostic performance. On the meantime, there are still several limitations in the present work. First, the correlation between size and membrane proteins was obtained in a protein-by-protein manner, which is not ideal for this application. This could be improved by combining the total internal reflection fluorescence mode[28, 29] and the iPM mode to simultaneously detect multiple membrane proteins and sizes at the single sEV level. Second, this work presented the first proof-of-concept study with cell lines and spiked samples. Further validation with clinical samples will be required to evaluate its potential in cancer diagnosis, which is currently undergoing.

290   **Materials and Methods**

291   **iPM system.** The iPM system was built on an inverted total internal reflection

292   fluorescence microscope (TIRFM) (Olympus IX83) using a 60 × oil immersion

293   objective (N.A. = 1.49). The surface plasmons were stimulated via Kreschmenn

294   configuration by a laser beam at 637 nm (OBIS 637 nm LX FP 100 mW) at a highly

295   inclined incident angle close to SPR dip angle. The real-time images of sEV were

296   recorded by a sCMOS camera (Prime TM; Photometrics). A motorized XY stage (Ludl

297   Electronic Products, Ltd.) was incorporated on the microscope to translate the sensor

298   chip.

299   **iPM sensor chips and surface modifications.** The sensor chips were 12-542-B

300   (Thermo Fisher) glass coverslips coated with 3 nm of chromium and 47 nm of Au. The

301   chips were cleaned first with deionized water and ethanol for three times, and dried by

302   nitrogen gas. After a quick hydrogen flame treatment, the sensor chip was immediately

303   immersed in modification buffer for 12 h. The modification buffer contained 1μM

304   aptamer (Sangon Biotech, China) 5uM Tris (2-carboxyethyl) phosphine (TCEP, Sigma)

305   and 1μM 6-Mercapto-1-Hexanol (MCH, Sigma). The chip was rinsed for three times

306   with 1× PBS buffer to remove unbound aptamers, and 50 μL of bull serum albumin

307   (BSA, Sigma) solution (1% w/v) was added to further block the residual active sites for

308   5 min. For positive-charge modification, the chip was treated with hydrogen flame and

309   immediately submerged in 10 mM HS-PEG-NH$_2$ (10,000 Da; Nanocs) water/ethanol

310   (1:1) solution overnight.

311   **Image processing**. The iPM images were processed offline with MATLAB R2018a

312   (MathWorks). Raw images were preprocessed by moving average with n = 10 frames.

313   The differential images between two adjacent average images were reconstructed with

314   home-developed codes. Briefly, by calculating the radius and center of the ring in k

315   space, the wave vector of single sEV was determined. Deconvolution was done in k

316   space using the point-spread function obtained experimentally, by aligning 30

317   individual images of 100-nm silica nanoparticles to the maximum intensity point, and

318   averaging after alignment. Then average intensity of the 3×3 pixels around the

319   brightest pixel of particle images was calculated as the particle intensity.

320   **Size calibration**. Silica nanoparticles (MikroNano Partikel GmbH) with the size of 30

321   nm, 50 nm, 70 nm, 100 nm and 160 nm were used to build the size-calibration curve.

322   Raw silica nanoparticles were diluted with $1\times$ PBS at 1:1000 vol/vol, and ultrasonicated

323   for 30 min to redisperse the single particles followed by centrifuging at 2000 rpm to

324   remove aggregates. 20 uL of nanoparticle solution was injected onto the positive-charge

325   modified sensor chips, and images were recorded for 2 min at 100 fps. Each experiment

326   was repeated in triplicates. The statistical histograms of silica nanoparticles were fitted

327   with a Gaussian function to determine the peak intensity values (mean $\pm$ SD, n > 150)

328   (Supplementary Fig. 4). The calibration curve was plotted as the intensity versus the

329   diameter of silica nanoparticles (Fig. 2f).

330   **Cell culture.** The human lung cancer cell line (A549, ATCC), hepatoma cell line

331   (HepG2, ATCC), breast cancer cell line (MCF-7, ATCC), and normal liver cell line (L-

332   02, ATCC) were cultured using high-glucose Dulbecco's modified Eagle's medium

333   (DMEM) (Hyclone) with 10% extracellular-vesicle-free fetal bovine serum (EV-free

334   FBS) (SeraPro) and 1% penicillin - streptomycin (Gibco). Prostate cancer cell line

335   (LNCaP, ATCC) was cultured in Roswell Park Memorial Institute 1640 (PRMI-1640)

336   (Hyclone) with 10% EV-free FBS (SeraPro) and 1% penicillin-streptomycin (Gibco).

337   Cells were cultured at 37 °C with 5% CO_2 in a humidified incubator (Thermo Fisher

338   Scientific). The cells were incubated in the T75 flask (Corning) with 30% confluent and

339   the culture medium was collected after 48 h culture when the cells were 70%-80%

340   confluent.

341   **Isolation of small extracellular vesicles.** sEV were isolated based on differential

342   centrifugation. Cell culture media (300 mL) was first centrifuged at 500g for 5 min,

343   followed by centrifugation at 2,000g for 45 min to remove cells. The treated medium

344   was centrifuged at 10,000g for 60 min. Then the supernatant was filtrated by 0.22 μm

345   membrane filtration (Millipore). Finally, the filtrate was ultracentrifuged at 100,000g

346   for 120 min. The sEV were washed by 50 mL 1× phosphate buffer saline (PBS,

347   Hyclone), followed by ultracentrifugation at 100,000g for 120 min. The purified sEV

348   were resuspended in 50 uL 1× PBS.

349   **Spiking test in human serum**. Human serum sample was collected from three healthy

350   volunteers with agreements at the Shanghai Sixth People's Hospital. Total volumes of

351   1 mL of clinical serum samples were first centrifuged at 2000g, and filtered through

352   0.22 μm pore filter (Millipore), then ultrafiltrated by 100 kDa ultrafiltration membrane

353   (Millipore) at 10,000g at 4 °C for 20 min. The EV-depleted serum was stored at -80 °C

354   before use. 10 uL A549 derived sEV was added to 90 uL EV-depleted serum to mimic

355   the real cancer-related serum with the final EV's concentration of 10^{10} / mL.

356   **NTA analysis**. The size distribution of sEV samples were characterized by NTA

357   (Particle tracking analyzer; Particle Metrix, PMX). All samples were diluted using PBS

358   to ~ 10^7 particles mL^{-1} before measurements. The data of size distribution were

359   analyzed with NTA software. The measurements were conducted at 25 °C.

360   **TEM**. 10 μL sEV sample (~ 10^{12} particles mL^{-1}) were directly absorbed on

361   Formvar/carbon-coated copper grids for two minutes. After blotting residual samples

362   with filter paper, 10 μL 1% phosphotungstic acid was dropped to stain sEV for 45

363   seconds followed by blotting the phosphotungstic acid with filter paper. After drying at

364   room temperature, the grids containing sEV were observed on Tecnai G2 spirit Biotwin

365   TEM (FEI) at 80 kV. For immunogold labeling of sEV sample derived from LNCaP,

366   CD63 aptamer-conjugated gold nanoparticles were incubated with sEV samples for 30

367   min at 4 °C, and the samples were dropped in grids for TEM detection. 10 uL CD63

368   aptamer (1uM) was mixed with 100 uL gold nanoparticles (4 ~ 10 nm, 2 mg/mL) at

369   4 °C for 12 h to prepare CD63 aptamer-conjugated gold nanoparticles, followed by

370   blocking active sites with BSA solution (1% w/v).

371   **Immunoblot analysis of sEV samples**. Isolated sEV samples and cells were treated

372   with radio immunoprecipitation assay (RIPA) lysis buffer including protease inhibitors

373 (Beyotime) with an ice bath for 30 min, followed by quantifying with a BCA assay.

374 Protein lysates were separated by sodium dodecyl sulfate-polyacrylamide gel

375 electrophoresis (SDS-PAGE), followed by transferring to polyvinylidene fluoride

376 (PVDF) membrane. The transferred PVDF membranes were blocked using 5% non-fat

377 dry milk in TBST buffer (TBS powder, Servicebio, 0.05% Tween-20) at room

378 temperature for 1 h. Then blocked membranes were immunoblotted with a panel of

379 primary antibodies including anti-Alix (Santa Cruz, sc-7964), anti-Tsg101 (Santa Cruz,

380 sc-7964), anti-Calnexin (Abcam, ab133615), anti-CD63 (NOVUS, NBP2-4225B), anti-

381 PTK7 (BBI, D199285-0100), anti-PSMA (Abcam, ab79542), anti-HER-2 (Abcam,

382 ab134190), anti-EpCAM (BBI, D263391) overnight at 4 °C. Followed by incubating

383 with corresponding HRP-conjugated secondary antibody for 1 h at 37 °C, the

384 membranes were washed three times for 10 min at room temperature with TBST buffer.

385 Finally, the western blot images were recorded on a gel image system (Tanon).

386 **Data analysis**.   The expression levels of target markers were defined by normalizing

387 the target-associated number recorded to those of total number of sEV. The total

388 number of sEV was measured by counting the number of sEV binding to the positive-

389 charged sensor surfaces. The protein levels of total sEV and three small-EVs subtypes

390 were normalized by subtracting the 2.5th percentile value and dividing by (97.5th

391 percentile value–2.5th percentile value). These normalized data were directly used for

392 LDA-based classification. Z-score were calculated by protein levels subtracted by mean

393 and divided by row standard deviation. The significance of the difference between the

394 sEV from cancer cell lines and normal cell line using individual protein marker was

395 calculated using a two-tailed, heteroscedastic t-test (**Fig. 3c**). The significance of the

396 difference between the sEV from five cell lines using individual protein marker was

397 calculated using a two-tailed, heteroscedastic

398 **The artificial intelligence algorithm.**

399 The artificial intelligence algorithm developed here is based on Python 3.7. Because

400 the sizing accuracy of iPM system is 10 nm, the data of SEVEN between 30 to 160 nm

401 were re-calculated into thirteen subgroups at the interval of 10 nm. Theoretically, there

402 are totally 2^{12} possibilities of subsets we can choose. Hill climbing algorithm was a

403 random local search optimization algorithm for nonlinear objective functions, which

404 was used to search for the locally optimal solution. Basically, hill climbing algorithm

405 includes the following steps. 1) a group of subsets was randomly set as the initial point

406 and its classification accuracy calculated by LDA was set as current best solution. 2)

407 the next new point was defined by the greedy strategy of hill climbing algorithm. And

408 the new classification accuracy was obtained. 3) the new classification accuracy was

409 compared with the previous one. If the new classification accuracy was equal to or

410 bigger than the previous one, the former point was abandoned and the latter was set as

411 the current point, and vice versa. Then repeat step 2 and step 3 to quickly find the

412 optimal solution.

413

423
424

425 **References**

426 1.   van Niel, G., D'Angelo, G. & Raposo, G. Shedding light on the cell biology of
427   extracellular vesicles. *Nat Rev Mol Cell Biol* **19**, 213-228 (2018).

428 2.   LeBleu, V.S. & Kalluri, R. Exosomes as a multicomponent biomarker platform
429   in cancer. *Trends Cancer* **6**, 767-774 (2020).

430 3.   Mathieu, M., Martin-Jaular, L., Lavieu, G. & Thery, C. Specificities of secretion
431   and uptake of exosomes and other extracellular vesicles for cell-to-cell
432   communication. *Nat Cell Biol* **21**, 9-17 (2019).

433 4.   Thery, C., Zitvogel, L. & Amigorena, S. Exosomes: composition, biogenesis
434   and function. *Nat Rev Immunol* **2**, 569-579 (2002).

435 5.   Hoshino, A. et al. Tumour exosome integrins determine organotropic metastasis.

436   *Nature* **527**, 329-335 (2015).

437   6.   Wortzel, I., Dror, S., Kenific, C.M. & Lyden, D. Exosome-mediated metastasis:
438   communication from a distance. *Dev Cell* **49**, 347-360 (2019).

439   7.   Gyuris, A. et al. Physical and molecular landscapes of mouse glioma
440   extracellular vesicles define heterogeneity. *Cell Rep* **27**, 3972-3987 (2019).

441   8.   Hoshino, A. et al. Extracellular vesicle and particle biomarkers define multiple
442   human cancers. *Cell* **182**, 1044-1061 e1018 (2020).

443   9.   Kalluri, R. & LeBleu, V.S. The biology, function, and biomedical applications
444   of exosomes. *Science* **367** (2020).

445   10.   Giulietti, M. et al. Exploring small extracellular vesicles for precision medicine
446   in prostate cancer. *Front Oncol* **8**, 221 (2018).

447   11.   Whiteside, T.L. Validation of plasma-derived small extracellular vesicles as
448   cancer biomarkers. *Nat Rev Clin Oncol* **17**, 719-720 (2020).

449   12.   Liu, C. et al. lambda-DNA- and aptamer-mediated sorting and analysis of
450   extracellular vesicles. *J Am Chem Soc* **141**, 3817-3821 (2019).

451   13.   Tian, F. et al. Protein analysis of extracellular vesicles to monitor and predict
452   therapeutic response in metastatic breast cancer. *Nat Commun* **12**, 2536 (2021).

453   14.   Liu, C. et al. Low-cost thermophoretic profiling of extracellular-vesicle surface
454   proteins for the early detection and classification of cancers. *Nat Biomed Eng* **3**,
455   183-193 (2019).

456   15.   Zhang, H. et al. Identification of distinct nanoparticles and subsets of
457   extracellular vesicles by asymmetric flow field-flow fractionation. *Nat Cell Biol*
458   **20**, 332-343 (2018).

459   16.   Bordanaba-Florit, G., Royo, F., Kruglik, S.G. & Falcon-Perez, J.M. Using
460   single-vesicle technologies to unravel the heterogeneity of extracellular vesicles.
461   *Nat Protoc* **16**, 3163-3185 (2021).

462   17.   Kowal, J. et al. Proteomic comparison defines novel markers to characterize
463   heterogeneous populations of extracellular vesicle subtypes. *Proc Natl Acad Sci*
464   *U S A* **113**, E968-977 (2016).

465   18.   Zheng, H. et al. Deconstruction of heterogeneity of size-dependent exosome
466   subpopulations from human urine by profiling *N*-glycoproteomics and
467   phosphoproteomics simultaneously. *Anal Chem* **92**, 9239-9246 (2020).

468   19.   Guan, S. et al. Size-dependent sub-proteome analysis of urinary exosomes. *Anal*
469   *Bioanal Chem* **411**, 4141-4149 (2019).

470   20.   Wu, M. et al. Isolation of exosomes from whole blood by integrating acoustics
471   and microfluidicss. *Proc Natl Acad Sci U S A* **117**, 28525 (2020).

472   21.   Zhang, H. & Lyden, D. Asymmetric-flow field-flow fractionation technology
473   for exomere and small extracellular vesicle separation and characterization.
474   *Nature Protocols* **14**, 1027-1053 (2019).

475   22.   Chen, Y. et al. Exosome detection via the ultrafast-isolation system: EXODUS.
476   *Nat Methods* **18**, 212-218 (2021).

477   23.   Hendrix, A. The nature of blood(y) extracellular vesicles. *Nat Rev Mol Cell Biol*
478   **22**, 243 (2021).

479   24.   Yang, Y. et al. Interferometric plasmonic imaging and detection of single

480   exosomes. *Proceedings of the National Academy of Sciences* **115**, 10275-10280
481   (2018).

482   25.   Yang, Y., Zhai, C., Zeng, Q., Khan, A.L. & Yu, H. Multifunctional detection of
483   extracellular vesicles with surface plasmon resonance microscopy. *Analytical*
484   *Chemistry* **92**, 4884-4890 (2020).

485   26.   Thery, C., Amigorena, S., Raposo, G. & Clayton, A. Isolation and
486   characterization of exosomes from cell culture supernatants and biological
487   fluids. *Curr Protoc Cell Biol* **Chapter 3**, Unit 3 22 (2006).

488   27.   Thery, C. et al. Minimal information for studies of extracellular vesicles 2018
489   (MISEV2018): a position statement of the International Society for
490   Extracellular Vesicles and update of the MISEV2014 guidelines. *J Extracell*
491   *Vesicles* **7**, 1535750 (2018).

492   28.   Zhou, S. et al. Accurate cancer diagnosis and stage monitoring enabled by
493   comprehensive profiling of different types of exosomal biomarkers: surface
494   proteins and miRNAs. *Small* **16**, e2004492 (2020).

495   29.   Xiao, X. et al. Intelligent Probabilistic System for Digital Tracing Cellular
496   Origin of Individual Clinical Extracellular Vesicles. *Anal Chem* **93**, 10343-
497   10350 (2021).

498